Structure and Dynamics of a Helical Hairpin and Loop Region in Annexin 12: A Site-Directed Spin Labeling Study†

J. Mario Isas,[‡,§] Ralf Langen,[§,||] Harry T. Haigler,*[,‡] and Wayne L. Hubbell*[,⊥]

Department of Physiology and Biophysics, University of California, Irvine, California 92697, Department of Biochemistry and Molecular Biology, University of Southern California, Los Angeles, California 90033, and Jules Stein Eye Institute and Department of Chemistry and Biochemistry, University of California, Los Angeles, California 90095-7008

Received September 27, 2001; Revised Manuscript Received December 4, 2001

ABSTRACT: A 30-residue nitroxide scan encompassing a helical hairpin and an extended loop in soluble annexin 12 (helices D and E in repeat 2; residues 134−163) has been analyzed in terms of nitroxide side chain mobility and accessibility to collision with paramagnetic reagents (Π). Values of Π for both O_2 and a Ni(II) metal complex (NiEDDA) are remarkably well correlated with the fractional solvent accessibility of the native side chains at the corresponding positions computed from the known crystal structure. This result demonstrates the utility of Π as an experimental measure of side chain accessibility in solution, as well as the lack of structural perturbation due to the presence of the nitroxide side chain. The pattern of side chain mobility is also in excellent agreement with predictions from the crystal structure. The results presented here extend the correlations between mobility and structure described in earlier work on other helical proteins, and suggest their generality. The periodic dependence of Π and mobility along the sequence of annexin 12 reveals the helical segments and their orientation in the fold, as expected for a nonperturbing nitroxide side chain. However, these data do not distinguish the helix−loop−helix motif from a continuous helix, because immobilized side chains in the short loop sequence maintain the periodicity. As shown here, the ratio of Π values for O_2 and NiEDDA clearly delineates the loop region, due to size exclusion effects between the two reagents. A new feature evident in a nitroxide scan through multiple secondary elements is a modulation of the basic Π and mobility patterns along the sequence, apparently due to differences in helix packing and backbone motion. Thus, in the short helix D, residues are consistently more mobile and accessible throughout the sequence compared to the residues in the longer, less-solvated and more ordered helix E.

Site-directed spin labeling (SDSL)[1] has become a powerful new tool for probing the structure of both water-soluble and membrane proteins at the level of the backbone fold (*1*−*5*). The basic strategy of SDSL involves the labeling of engineered cysteine residues with a nitroxide reagent to generate a disulfide-linked nitroxide side chain. The most commonly employed side chain is designated R1 (Figure 1).

The shape of the electron paramagnetic resonance spectrum of R1 in a protein encodes information on the side chain mobility, while the change in the R1 spin−lattice relaxation time due to the presence of a paramagnetic reagent in solution measures the diffusion-limited collision rate of R1 with the reagent. Experimentally, collision rates are measured by the proportional quantity Π, the "accessibility parameter" (*6*). As shown in this study, Π(O_2) and Π(NiEDDA) are valid experimental measures of side chain solvent accessibility.

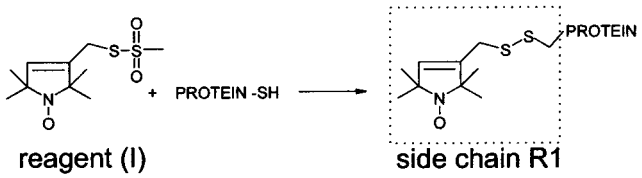

FIGURE 1: Reaction of the spin-label reagent (I) to give the nitroxide side chain designated R1.

A goal of site-directed spin labeling is to decipher patterns of mobility and Π in terms of secondary structure, tertiary structure, and protein dynamics. For example, the identity of regular secondary structure as well as features of the tertiary fold can be extracted from the periodic variation of R1 mobility and accessibility along a sequence in a nitroxide scanning experiment. This strategy has proven to be a robust method of determining sequence-correlated secondary structure, and many examples are in the literature (*6*−*17*). The mobility of R1 reflects internal modes (torsional oscillations about bonds) and segmental motions of the backbone to

† This work was supported by National Institutes of Health Grants GM-55651 (H.T.H.), GM63915 (R.L.), and EY05216 (W.L.H.), the Jules Stein Professor Endowment (W.L.H.), the Bruce Ford and Anne Smith Bundy Foundation (W.L.H.), and Research to Prevent Blindness (W.L.H.).

* To whom correspondence should be addressed. W.L.H.: Jules Stein Eye Institute, UCLA School of Medicine, 100 Stein Plaza, Los Angeles, CA 90095-7008; phone, (310) 206-8830; fax, (310) 794-2144; e-mail, hubbellw@jsei.ucla.edu. H.T.H.: Department of Physiology and Biophysics, University of California, Irvine, CA 92697; phone, (949) 824-6304; fax, (949) 824-8540; e-mail, hhaigler@uci.edu.

‡ University of California, Irvine.

§ These authors contributed equally to this work.

|| University of Southern California.

⊥ University of California, Los Angeles.

[1] Abbreviations: NiEDDA, Ni(II) ethylenediaminetetraacetate; EPR, electron paramagnetic resonance; f_{SA}, fractional solvent accessibility; SDSL, site-directed spin labeling; T4L, T4 lysozyme.

10.1021/bi011856z CCC: $22.00
Published on Web 01/11/2002

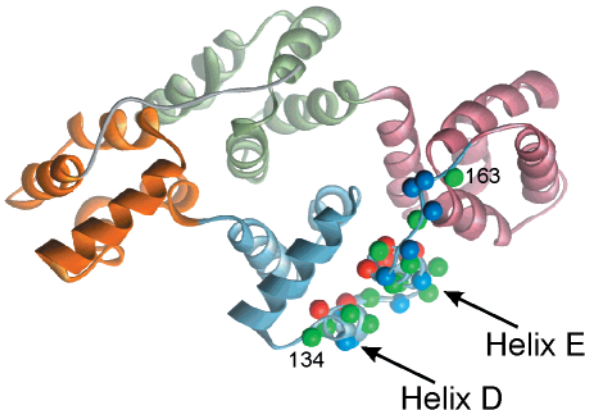

FIGURE 2: Crystal structure of an annexin 12 monomer (*22*), viewed from the concave side of the molecule. The amino-terminal domain is gray, and each of the four repeats in the core domain is a different color. Each repeat contains five helices (A−E), and helices D and E are labeled in repeat 2. Sites of spin-labeled residues 134−163 are denoted by solid spheres on the α-carbons. The α-carbons are color-coded according to the solvent accessibility (see the text).

which the side chain is attached. The internal modes are dramatically modulated by tertiary interactions, and systematic studies in T4 lysozyme as a model protein showed that interhelical loop sites, helix surface sites, tertiary contact sites, and buried sites were partially resolved by differences in R1 mobility, largely due to this effect (*14*). Interestingly, the EPR spectra for R1 at helix surface sites where no tertiary contact interactions are made are site-specific, yet largely independent of the nature of nearest-neighbor mutations. Such site-specific effects at noninteracting helix surface sites appear to be related to backbone motions in the nanosecond regime (*14*, *18*).

In the study presented here, correlations of both R1 accessibility and mobility to protein structure and dynamics are extended to include a 30-residue continuous scan through a helical hairpin in annexin 12. Annexins are a family of soluble proteins that bind to phospholipid bilayers in the presence of Ca^{2+} (*19*, *20*). Typically, they are made up of four highly homologous and conserved repeats. High-resolution crystal structures are available for the soluble form of several annexins (*21*). Not surprisingly, the structures of these different annexin gene products are nearly superimposable, composed of individual repeats that themselves are nearly identical in structure. The latter point is illustrated (Figure 2) in the crystal structure of annexin 12 (*22*). Each of the four repeats (represented by different colors) of annexin 12 contains five helices. Four of these helices (A, B, D, and E) form a helical bundle on top of which sits helix C. The loops connecting helices A and B and helices D and E are located on the opposing, convex side of the protein where they are believed to mediate the Ca^{2+}-dependent membrane interaction.

The nitroxide scan analyzed here, 134R1−163R1 in annexin 12, includes the hairpin of helices D and E in the second repeat and parts of the loop connecting repeats 2 and 3 (Figure 2). The results of the study reveal a remarkable correspondence between the collision rate of R1 with the paramagnetic reagents O_2 and NiEDDA, measured by Π, and the fractional solvent accessibility of the native side chain determined from the crystal structure. As anticipated, periodic variations in mobility and Π identify helices D and E. However, the periodic property alone does not locate the position in sequence of the connecting loop, but this can be accomplished with the contrast parameter $\Phi = \ln[\Pi(O_2)/\Pi(\text{NiEDDA})]$, previously employed to estimate the depth of immersion for nitroxides in bilayers (*23*).

The mobility of R1 throughout the sequence also accurately reflects the structural model of annexin derived from crystallography, and the relationship of mobility to structure is very similar to that found for T4L (*14*), suggesting generality of the results. Moreover, the dynamic mode of the R1 side chain at noninteracting helix surface sites is the same as that previously characterized in T4L (*18*) and colicin E1 (*10*). The site-dependent variation in Π and R1 mobility, the latter assessed by both order parameter and the inverse central line width, is interpreted to reflect a generally greater segmental motion in the short D helix than in the longer E helix, a conclusion in accord with a recent NMR study of an isolated repeat of annexin I (*24*).

MATERIALS AND METHODS

Protein Expression and Purification. A series of 30 single-cysteine substitution mutants that correspond to residues 134−163 of annexin 12 were constructed as previously described (*25*, *26*). All mutations were confirmed by DNA sequencing using a Sequenase 2.0 kit (Amersham). The annexin 12 mutants were expressed in recombinant bacteria and purified by reversible Ca^{2+}-dependent binding to phospholipid vesicles followed by column chromatography as previously described (*25*).

Spin Labeling, EPR Spectroscopy, and Fractional Solvent Accessibility. The methods used to modify cysteine residues with the nitroxide reagent (1-oxy-2,2,5,5-tetramethylpyrrolinyl-3-methyl)methanethiosulfonate (a generous gift from K. Hideg, University of Pécs, Pécs, Hungary) were as described previously (*25*). Spin-labeled mutants of annexin 12 are designated by giving the sequence position of the cysteine substitution followed by the code of the nitroxide spin-label, R1. Spin-labeled proteins were stored in Hepes buffer (20 mM, pH 7.4) containing NaCl (100 mM). Prior to use, the spin-labeled proteins were concentrated in a Microcon YM-10 apparatus (Amicon) using a tabletop centrifuge.

EPR experiments were performed on spin-labeled annexin 12 mutants (100−200 μM protein) in Hepes buffer (20 mM, pH 7.4) containing NaCl (100 mM). Samples analyzed for mobility also contained sucrose (30%, w/w) to reduce protein rotational motion and thereby minimize the contribution of protein rotation to the EPR spectral line shape (*14*). EPR spectra were obtained using a Varian model E-109 spectrometer fitted with a loop gap resonator (*27*). All spectra were obtained at a 2 mW incident microwave power and a field modulation of ~1 G (1 G = 0.1 mT). The Π parameters for both O_2 and NiEDDA were measured using the power saturation method previously described (*28*, *29*). The concentration of O_2 was that in equilibrium with air at ambient temperature, and for NiEDDA was 3 mM. Mobility was estimated using both the inverse central line width (ΔH_o^{-1}) and the inverse spectral second moment ($\langle H^2 \rangle^{-1}$) as previously described (*14*).

The fractional solvent accessibility for native residues in annexin 12 was computed from the crystal structure of a monomer of the crystallographic hexamer (*22*) (PDB entry

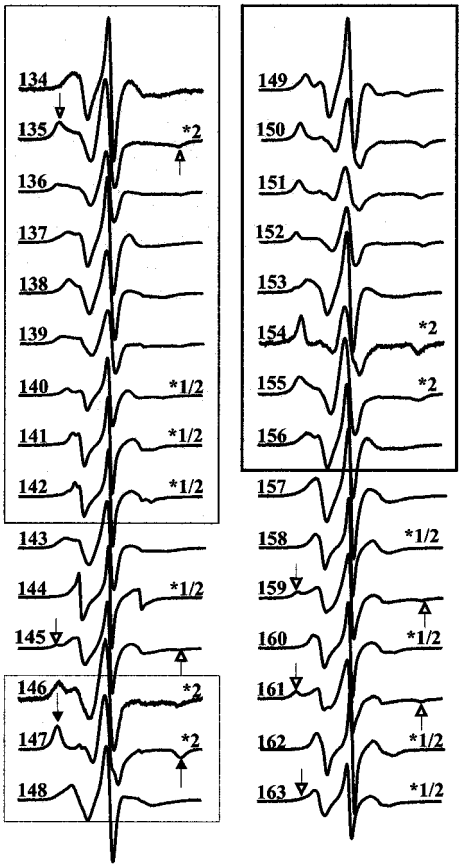

FIGURE 3: EPR spectra of annexin 12 containing the R1 nitroxide side chain at the indicated sites. The spectra are normalized to correspond to the same number of spins. For convenience of presentation, the amplitudes of some spectra were either increased or reduced by a scaling factor shown to the right of the spectra. Shaded boxes represent the extent of helices D and E. The filled arrows in the spectrum for 147R1 identify the hyperfine extrema in the powder line shape. The empty arrows in other spectra identify a spectral component corresponding to an immobilized state of the nitroxide. All annexin samples were in 30% sucrose solution at pH 7.4, and the magnetic field scan width is 100 G.

1AEI) using the program MolMol (*30*) and a probe radius of 1.4 Å.

RESULTS

Figure 3 shows the EPR spectra obtained for each spin-labeled annexin 12 in the sequence of residues 134−163 in a 30% sucrose solution. The shaded regions indicate the extent of helices D and E based on the crystal structure model. For R1 at each site, the accessibility parameters Π-(O_2) and Π(NiEDDA) were measured. The R1 mobility was estimated from the spectral line shape parameters ΔH_0^{-1} and $\langle H^2 \rangle^{-1}$ or from apparent order parameters. The accessibility parameters are considered first, because they can be directly and quantitatively compared with the crystal structure data.

Accessibility to Collision with O_2 and NiEDDA. Figure 4a (top panel) shows a plot of Π(O_2) and Π(NiEDDA) as a function of sequence position. As is evident, there is a regular periodic variation in both quantities throughout the sequence of residues 134−156 that encompasses helices D and E and the interconnecting loop, but is sharply attenuated and modified upon entering the connecting loop of residues 157−163. The Fourier transform of the Π(NiEDDA) data for the helical hairpin of residues 134R1−156R1 reveals a dominant component with a period of ≈3.8 residues (frequency of 0.26 residue^{-1}), close to that of 3.6 residues/turn for a regular helix (Figure 4b, top panel). A second component with a period of 23 residues (frequency of 0.043 residue^{-1}), the length of the scan, corresponds to a low-frequency modulation of the helical frequency. This is seen in the data as a background "roll". These two frequency components are shown in Figure 4b (bottom panel), superposed on the Π-(NiEDDA) data. The origin of the low-frequency component is the generally greater accessibility of residues in helix D and the loop than in helix E. In particular, there is a gradient of increasing residue accessibility along helix D from residue 134 to 141 and into the loop, and then a decrease to the center of helix E, followed by an increasing gradient to the end of the helix. Because the helices are not too different in length, this gives rise to the sinusoidal modulation with a period equal to the length of the sequence. Clearly, analysis of the Π(O_2) data leads to the same conclusions.

It is intuitively reasonable that the collision rates of water-soluble paramagnetic reagents with R1 should be correlated with the solvent accessibility of the R1 side chain. However, it is not obvious to what extent they are related to the solvent accessibility of the native side chains at the corresponding sites. To explore this issue, Figure 4a (middle panel) shows the fractional solvent accessibility (f_{SA}) for each native residue through the sequence computed from the crystal structure using a probe radius of 1.4 Å. A monomer from the crystallographic hexamer was used for these calculations (*22*). The periodicity and relative amplitudes of f_{SA} with sequence position strongly resemble those features for both Π(O_2) and Π(NiEDDA). The few exceptions are such that Π is relatively greater than f_{SA}, and these occur at glycine residues (G145 and G157) or at sites where the native side chains have particular interactions (Q148, R159, and E163) that reduce their solvent accessibility relative to the R1 side chain (see the Discussion). The close correspondence of f_{SA} and Π values is further emphasized by a comparison of the Fourier transform of f_{SA} shown in Figure 4c with that of Π-(NiEDDA) (Figure 4b, top panel). Again, the dominant component corresponds to a period of 3.8 residues. The low-frequency component with a period of 23 residues is also present, but slightly attenuated relative to that for Π-(NiEDDA).

For convenience in discussions to follow, the topography of R1 residues in the protein fold will be classified in part according to their solvent accessibility in the crystal structure measured by f_{SA}. Thus, residues with an f_{SA} of ≤0.05 will be defined as "buried", those with an f_{SA} between 0.05 and 0.25 as "partially solvent-accessible", and those with an f_{SA} of >0.25 as "solvent-exposed" (see Figure 4a, middle panel). These definitions are somewhat arbitrary, but they represent the location of the native side chain in the structure reasonably well. Sites that are partially solvent accessible are generally those that make contact interactions and vice versa, and sites that are solvent-exposed are on the surface of the protein. In previous publications, such sites were termed "contact" and "surface" sites, respectively, and this terminology will be retained here. The f_{SA} values in Figure 4a (middle panel) are color-coded according to this assignment.

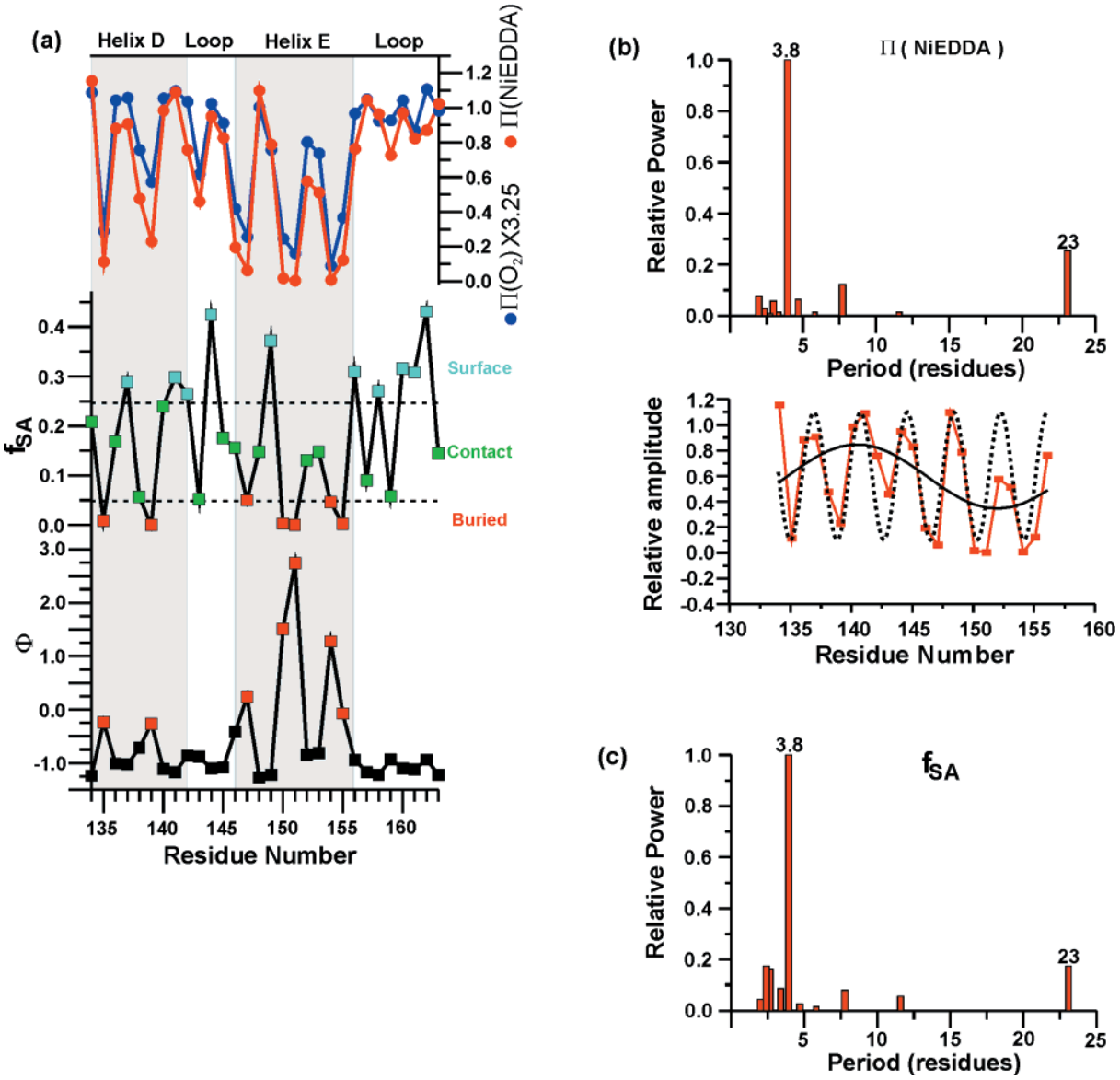

FIGURE 4: Sequence dependence of R1 accessibility. (a, top panel) $\Pi(O_2)$ (blue) and Π(NiEDDA) (red) as a function of sequence. (a, middle panel) Fractional solvent accessibility computed from the crystal structure as a function of sequence. The horizontal dashed lines at 0.05 and 0.25 define the boundaries between "buried", "partially solvent accessible" (contact), and "solvent accessible" (surface) residues (see the text). Individual residues are color-coded according to this assignment where red, green, and blue indicate buried, contact, and surface locations, respectively. The same color code is used in Figure 2. (a, bottom panel) Function Φ as a function of sequence. (b, top panel) Fourier transform power spectrum of Π(NiEDDA), plotted as a function of period. (b, lower panel) Π(NiEDDA) data (red squares) plotted together with the component of period 3.8 (dotted trace) and the component of period 23 (solid trace) present in the Fourier transform of the data. (c) Fourier transform power spectrum of the fractional solvent accessibility, plotted as a function of period.

The regular periodicity of f_{SA}, $\Pi(O_2)$, and Π(NiEDDA) throughout the helix−turn−helix sequence of residues 134−156 indicates that the periodicity alone cannot in general distinguish an extended continuous helix from the helix−loop−helix structure. The problem stems from the fact that loop residues are not necessarily all highly exposed, and can be partially buried, extending the apparent helix periodicity through the loop region. In this case, it is loop residue 143 that is partially sequestered from solvent contact. However, the contrast function $\Phi = \ln[\Pi(O_2)/\Pi(\text{NiEDDA})]$ provides a means of identifying loop residues, as shown in Figure 4a (bottom panel). As previously pointed out, Φ is expected to be approximately constant for solvent-exposed and contact residues (*23*). Only for deeply buried residues does Φ increase dramatically due to the greater penetration of O_2 into the protein interior compared to the more polar, larger NiEDDA complex (*9*). This size exclusion effect is illustrated in Figure 5 for annexin 12, where it can be seen that the $\Pi(O_2)/\Pi$(NiEDDA) ratio is approximately the same for all sites except for deeply buried sites, where Π(NiEDDA) tends to zero while $\Pi(O_2)$ remains finite. Due to this effect, Φ is roughly constant except the value for deeply buried sites, where it increases steeply. As seen in Figure 4a (bottom panel), Φ clearly picks out the most buried residues on the inner surfaces of the helices, revealing the turns 2 and 3 of helices D and E, respectively. On the other hand, Φ changes little through the loop regions, clearly marking their location. Apparently, residue 143R1 in the loop is not sufficiently buried for the size exclusion effect to be large, an effect possibly related to loop dynamics.

It is interesting to note that both Π and Φ resolve accessibility differences between helices D and E, most

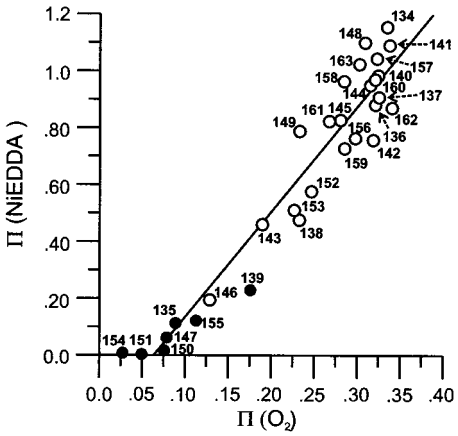

FIGURE 5: Plot of Π(NiEDDA) vs Π(O_2) for R1 residues in the sequence of residues 134−163. Contact and surface residues, defined by the data depicted in Figure 4a (middle panel), are denoted with empty circles and buried residues with filled circles.

notably on their buried faces. As discussed above, the low-frequency component in the Fourier transform of Π-(NiEDDA) arises from such differences. In addition, the Φ values for buried sites 135R1 and 139R1 in helix D are clearly smaller than those for buried residues 147R1, 151R1, and 154R1 in helix E, indicating that the size exclusion effect is less for the former case. Taken together, these results suggest a looser packing of helix D compared to E, with a greater solvent penetration.

Mobility. The mobility of the R1 residues can be qualitatively assessed from the features of the EPR line shapes shown in Figure 3. For example, R1 residues that are in the slow motional limit are readily identified by the so-called "powder" line shape with well-resolved hyperfine extrema whose separation depends on solvent polarity (*31*). In helix E, residues 147R1, 150R1, 151R1, and 154R1 have a powderlike line shape and are hence strongly immobilized in the protein. The splitting between the outermost hyperfine extrema for each (illustrated by solid arrows for 147R1 in Figure 3) is ≈68 G, suggesting an apolar environment (*32*) consistent with the protein interior. These positions correspond exactly with those of buried native residues, identified by the fractional solvent accessibility (Figure 4a, middle panel), and with those of lowest Π (Figure 4a, top panel). Residue 155R1 is also identified as a buried site in the structure. For this residue, the EPR spectrum reflects multiple states of different mobility, as judged by diffuse spectral intensity in the region between the low-field and center resonance lines. However, the dominant component corresponds to the expected immobilized state of the R1 residue. In short helix D, none of the R1 residues, including those at buried sites 135 and 139, have simple spectra characteristic of strong immobilization. Rather, these buried sites have multiple components, one of which corresponds to the anticipated immobilized state (empty arrows, Figure 3).

At the other extreme, R1 residues with high mobility are readily identified by the narrow overall breadth and sharp features in the EPR spectra. For example, the sites at which the native residues have the highest solvent accessibility (surface sites) are also the sites at which R1 residues have among the sharpest spectral features and hence the highest mobility (residues 137, 138, 141, 142, 144, 149, 156, 158, 160, and 162). Residues 157, 161, and 163 are exceptions to be discussed below.

Thus, qualitatively, the pattern of R1 side chain mobility mirrors the solvent accessibility and the protein structure in the crystal. A more quantitative evaluation of mobility can be based on the width of the central resonance line ($m_I = 0$) of R1. The line width is determined by the nitroxide *g*-factor anisotropy and the rate and geometry of molecular motion. For isotropic motion, the line width is sensitive to rotational correlation times in the range of ≈1−30 ns. The inverse central line width, ΔH_o^{-1}, is an increasing function of mobility in this domain, and has been previously employed as a semiquantitative measure of nitroxide mobility (*14*). Figure 6a shows the dependence of ΔH_o^{-1} on sequence for the nitroxide scan from 134R1 to 163R1. As for f_{SA}, Π(O_2), and Π(NiEDDA), there is a regular periodicity extending through the helix−loop−helix sequence of residues 134R1−156R1, and the residues corresponding to the maxima and minima of mobility correspond closely to those for the Π parameters. One exception is residue 136R1 that has the unusual combination of low mobility and high accessibility. The α-carbon of residue 136 resides on a contact surface of helix D, but the native Glu side chain projects out toward the solution. Apparently, R1 adopts a similar configuration, with the nitroxide ring solvent-exposed, but immobilized by relatively strong contact interactions.

The Fourier transform of the ΔH_o^{-1} data is shown in Figure 6b, and the major components of the transform are shown plotted with the mobility data as a function of sequence in Figure 6c. As for Π and f_{SA}, the major components have periods of 3.8 residues and 23 residues, respectively. Again, the period of 3.8 identifies the D and E helical segments, but it is not possible to distinguish the helix−loop−helix motif from a continuous helix based on periodic properties alone. The low-frequency modulation of the mobility data with a period of 23 residues reflects the differential dynamics of side chains in helices D and E, just as the low-frequency modulation of the accessibility data reflected a differential accessibility in those helices. Thus, there is an increasing gradient of mobility from the beginning of helix D at residue 134 to the center of the turn, and a decreasing gradient of mobility from the turn to helix E. However, the relative contribution of the low-frequency mode in the power spectrum is considerably greater than for the Π(NiEDDA) case, indicating that ΔH_o^{-1} is a more sensitive measure of helix dynamics.

Mobility measured by ΔH_o^{-1} is comparatively high at loop sites (Figure 6a). However, several of the loop sites have low values of f_{SA} for the native residues, identifying them as inward-pointing side chains with significant contact interactions (Figure 4a, middle panel). Interestingly, these residues either are partially immobilized (143R1) or have two spectral components, one of which reflects a significant degree of ordering and immobilization (empty arrows in Figure 3 for 145R1, 159R1, and 161R1) due to contact interactions, and this population gives rise to the β-strand-like periodicity in the loop of residues 157−163 (Figures 4a and 6a). These latter residues are the same ones noted above at which there are significant differences between Π-(NiEDDA) and f_{SA}. The origin of this difference is that the method for determining Π values emphasizes the most exposed population at a site with multiple populations. Thus,

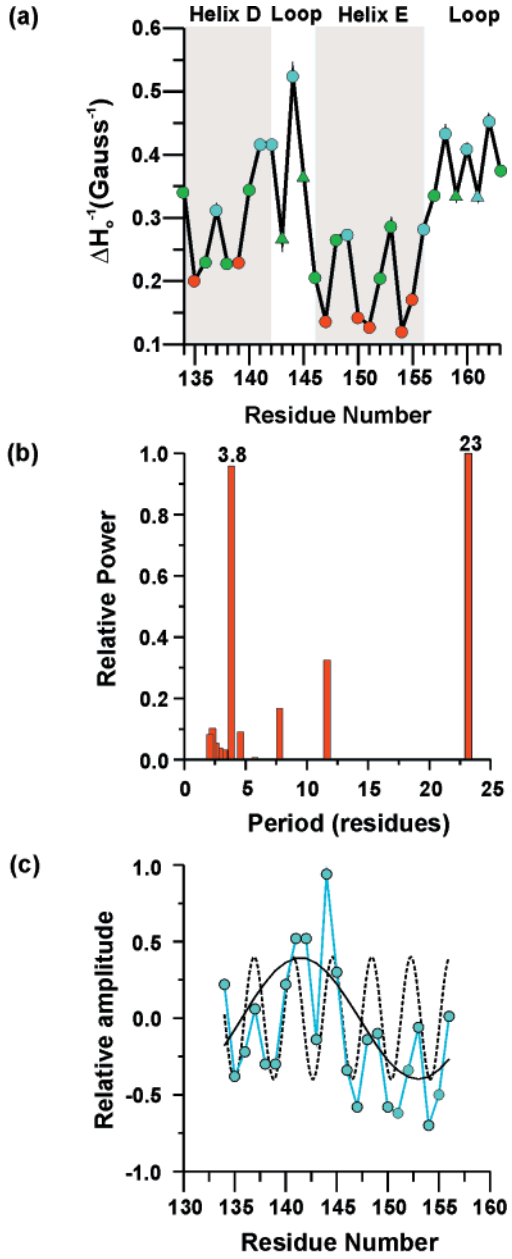

FIGURE 6: Sequence dependence of R1 mobility. (a) ΔH_o^{-1} as a function of sequence. The residues are color-coded according to the definitions in the legend of Figure 4a (middle panel). (b) Fourier transform power spectrum for the data in panel a, plotted as a function of period. (c) ΔH_o^{-1} data (blue circles), plotted together with the component of period 3.8 (dotted trace) and the component of period 23 (solid trace) present in the Fourier transform of the data.

Π overestimates the "average" degree of solvent exposure at such sites compared to f_{SA}. Loop residue 161R1 also shows two populations, but the native glutamic acid is highly solvent-exposed in the crystal structure. Nevertheless, it does face inward in the protein fold, and apparently, the uncharged and relatively hydrophobic R1 side chain can make contacts that were avoided by the highly solvated native residue.

Another measure of R1 mobility is the inverse second moment, $\langle H^2\rangle^{-1}$, which emphasizes contributions from outer hyperfine extrema in the spectrum. In previous work, a plot of ΔH_o^{-1} versus $\langle H^2\rangle^{-1}$ was found to map (group) side chains from different topographical regions of the protein fold into defined regions on the plot (*8*, *14*). In that work, as in the

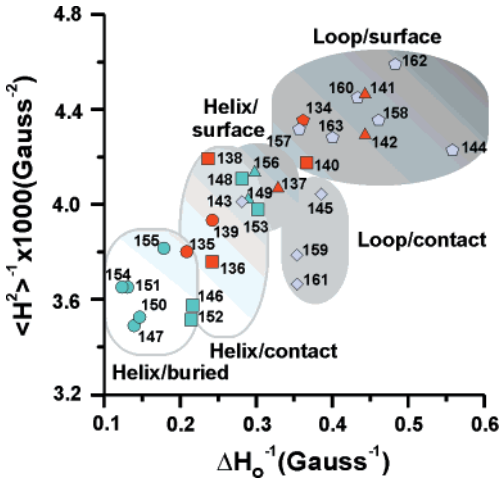

FIGURE 7: Mobility map (ΔH_o^{-1} vs $\langle H^2\rangle^{-1}$) for annexin 12. Helix/buried residues are denoted with circles, helix/contact residues with squares, helix/surface residues with triangles, loop/contact residues with diamonds, and loop/surface residues with pentagons. Residues in helix D are shown in red, those in helix E in blue, and those in loops in magenta.

work presented here, all sites were in helical segments or interconnecting loops, and the topographical regions were classified as buried, tertiary contact, surface, or loop regions. Figure 7 shows such a topographical map for the nitroxide scan in annexin 12, and it is evident that a similar grouping is possible with approximately the same boundaries. However, some refinements are indicated by the data presented here. In the T4L study, the loop sites were identified as a unique class because each loop that was investigated was fully solvent-exposed, and R1 residues within such loops had high values for both ΔH_o^{-1} and $\langle H^2\rangle^{-1}$. In annexin 12, the loops are not fully solvent-exposed, and some sites within loops have reduced accessibility and mobility (Figures 4a and 6a).

To accommodate this new class of sites and to generalize the earlier classification, the topographical classification of a side chain will be based on (1) the type of secondary structure and (2) the solvent accessibility of the side chain in the crystal structure. The coarse scale of solvent accessibility given above will be used, namely, buried, contact, and surface. Thus, the designation for R1 at a buried site on a helix will be "helix/buried", and that for R1 in a loop at a site with only partial solvent accessibility will be "loop/contact", and so forth. The topographical map of the annexin 12 sequence of residues 134−163 (Figure 7) reflects these definitions. These are coarse definitions, and subdivisions can be made as necessary. For example, any helix can be subdivided to distinguish internal, C-terminal, or N-terminal sites (*14*), and a β-strand can be an edge strand or a center strand.

It should be noted that the above classification does not imply that an R1 residue at a helix/surface site has no interaction with the environment. R1 at such sites may be interacting or noninteracting, depending on the potential for specific interactions of the R1 side chain with other residues in the immediate environment. Such interactions modulate the side chain mobility, and this is one of the reasons that helix/surface sites occupy an area on the plot of Figure 7 rather than a point. The noninteracting helix/surface site has a signature spectrum, illustrated in Figure 8 by that of 72R1

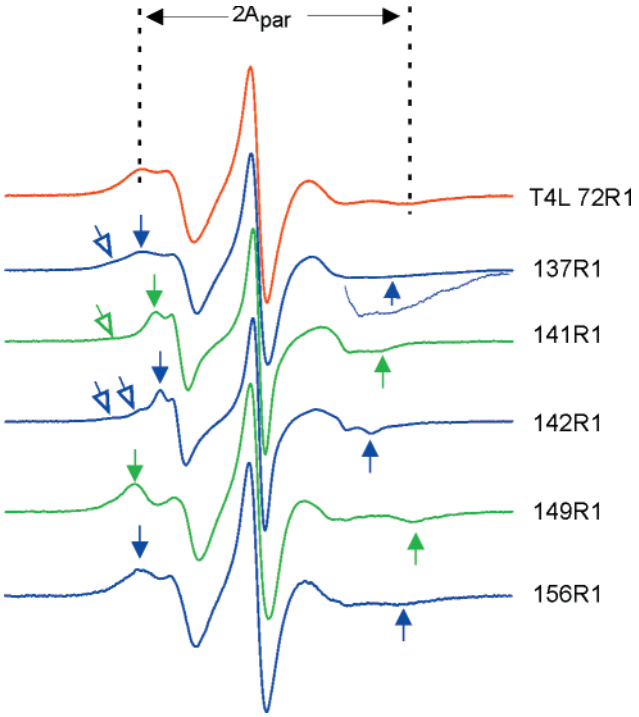

FIGURE 8: EPR spectra of the indicated helix/surface sites. 72R1 in T4L (red trace) is a noninteracting helix/surface site shown for reference. Dashed lines indicate the separation between the outer hyperfine extrema ($2A_{par}$) for 72R1. The other spectra are of R1 at the indicated sites in annexin 12. Filled arrows indicate the resolved outer hyperfine extrema in these spectra. Empty arrows indicate the low-field position of spectral components corresponding to relatively immobilized states. The high-field region of the spectrum of 137R1 is shown at high gain to reveal the high-field extreme.

from T4 lysozyme (*14*). This residue is among the most ordered for noninteracting helix/surface sites, and the spectrum is shown here as a reference. The structural and dynamical origin of this spectral line shape was studied in detail by simulation techniques (*18*). The spectrum corresponds to a single dynamic population undergoing anisotropic motion, and is characterized by well-resolved outer and inner hyperfine extrema. The large separation between the outer hyperfine extrema, designated $2A_{par}$, is identified in Figure 8. A single order parameter, S, and an anisotropic diffusion tensor can accurately account for such helix/surface site spectra. In an approximate effective Hamiltonian treatment, the positions of the hyperfine extrema can be reproduced with a single apparent order parameter, $S_{app} = (2A_{par} - {}^3/_2a_o)/(2A_{zz} - {}^3/_2a_o)$, where A_{zz} is the z principle value of the hyperfine tensor in the absence of motion and a_o is the isotropic hyperfine coupling constant in the same solvent which equals ${}^1/_3(A_{zz} + A_{xx} + A_{yy})$, where A_{zz} and A_{par} are determined and A_{xx} and A_{yy} are the principle x and y tensor values corresponding to A_{zz}]. For T4L 72R1, $S_{app} = 0.5$.

According to the crystal structure of annexin 12, the helix/surface sites are residues 137, 141, and 142 in helix D and residues 149 and 156 in helix E (Figure 4a). The spectra of R1 at these sites are compared in Figure 8. The line shapes of 149R1 and 156R1 in helix E are similar to that of T4L 72R1, and correspond to a single population of nitroxide undergoing anisotropic diffusion with S_{app} values of 0.6 and 0.5, respectively. For R1 on helix/surface sites in helix D, the spectra are more complex and reflect multiple components. In each case, one of the components has a line shape characteristic of the expected anisotropic motion with an order parameter lower than those in helix E (the hyperfine extrema corresponding to A_{par} are indicated with filled arrows in Figure 8). For these apparently noninteracting components, the apparent order parameters for 137R1, 141R1, and 142R1 are 0.45, 0.38, and 0.24, respectively. The more immobilized spectral components, identified with empty arrows in Figure 8, presumably arise from interactions with the protein environment.

DISCUSSION

Correlation of Solvent Accessibility and Mobility with Static Structure. This study examines the pattern of mobility and accessibility of the R1 side chain through a helix−loop−helix−loop sequence in annexin 12. The primary motivations were (1) to advance the technology of SDSL by providing a database for correlation of EPR parameters with protein structure and (2) to compare the solution structure of annexin 12 with that in the crystal as a prelude to future studies of the membrane-bound form of the protein. In previous studies in T4L, the mobility of R1 at various sites was correlated with regular secondary structure and salient features of the tertiary fold (*14*). In the study presented here, this work is extended to include a scan through a supersecondary structural element, the helix−loop−helix motif, and to include R1 accessibility data.

The data in Figure 4 reveal a striking similarity between the sequence dependence of Π values for both O_2 and NiEDDA and that of f_{SA}, particularly through the helical hairpin. This suggests that Π values are valid experimental estimates of the relative solvent accessibility of the native side chain at the corresponding site. Such a simple result is not necessarily anticipated, because R1 is larger than most of the native side chains, and at contact sites R1 could project either into the protein interior or into the solvent.

As mentioned above, exceptions to the correlation are observed and expected at glycine residues where the size difference of the side chains is at the extreme (residues 145 and 157). Other exceptions occur in the interdomain loop sequence from residue 157 to 163 where several of the EPR spectra exhibit two components corresponding to R1 populations with greatly differing mobilities (residues 159, 161, and 163). At such sites, the method of determining Π is heavily biased toward the most exposed site, overestimating the "average" Π value. Residue 145R1 also has two components, and this could contribute to the low Π values relative to f_{SA}. Finally, poor correlations between Π and f_{SA} may occur for particular cases where the native residue has specific interactions with the environment that reduce its solvent accessibility. For example, native arginine 159 projects into the protein interior, apparently in interaction with tyrosine 201. The R1 side chain does not experience the same interaction that would keep it completely buried, and this may be the origin of the two populations of R1 at this site.

The generality of the correlation between Π and f_{SA} remains to be seen, but similar results have been noted in colicin E1 (M. Vogelsang and W. Hubbell, unpublished data) and rhodopsin (C. Altenbach, J. Klein-Seetharaman, K. Cai, H. Khorana, and W. Hubbell, unpublished data). With an understanding of the limitations, the correlation provides a

simple means for comparing crystal and solutions structures using accessibility data from SDSL. It should also be mentioned that the data are consistent with the absence of significant structural perturbation by side chain R1. This point is further supported by the fact that all of the derivatives retained their ability to bind to phospholipid bilayers in a calcium-dependent manner (*26*).

As expected, the periodic dependence of mobility with sequence generally mirrors that of accessibility (Figures 4a and 6a). The "mobility map" for annexin 12 (Figure 6b) resolves the individual sites that were investigated into regions that closely correspond to topographical regions defined by the crystal structure. An exception is residue 161R1. Although the native glutamic acid points inward in the structure, the charged residue remains highly solvated. The R1 residue at this inward-facing site has numerous opportunities for interactions, and the spectrum reveals two components, one corresponding to a strongly immobilized site. Other exceptions involving residues in helix D will be discussed below in reference to backbone mobility.

The map for annexin 12 is very similar to that found for T4L (*14*), suggesting the generality of the correlation between R1 mobility and protein structure. However, a new topographical region is represented in annexin 12, the loop/contact region. In T4L, the loops that were investigated were completely solvent-exposed and the R1 residues in these regions were highly mobile. Although loops are generally solvent-exposed surface structures in protein folds, they may lie close to other structures. Hence, a loop residue facing another structure may interact and be at least partially immobilized. The fact that R1 can favorably interact with residues in its proximity is supported by the recent crystal structure analysis of spin-labeled T4 lysozyme mutants, which shows that the R1 side chain can engage in a variety of hydrophobic and hydrophilic interactions (*33*).

As mentioned above, several of the loop/contact R1 residues have two dynamic populations (residues 145, 159, 161, and 163). The most immobile population corresponds to R1 interacting with the protein, but this population is only weakly reflected in the ΔH_o^{-1} measure of mobility, which is heavily biased toward the most mobile component. Thus, ΔH_o^{-1} measures loop sites as relatively mobile (Figure 6a). On the other hand, the second moment measure of mobility emphasizes the most immobile component, and it is the second moment that resolves the loop/contact sites in the mobility map of Figure 7. The components of the loop/contact spectra reflecting the mobile population of R1 resemble the spectra of mobile loop sites in T4L. The high mobility of such sites was attributed to flexibility in the loop backbone structure (*14*).

In previous work, the periodic properties of Π and mobility along a sequence have been used to identify sequence-correlated secondary structure. However, the data presented above indicate that the existence of loop/contact (or loop/buried) sites makes it problematic to resolve unambiguously a helix−loop−helix motif from a continuous helix based on periodicity alone, because the loop/contact sites can extend the periodicity through the loop, if it is short. In such cases, the function Φ may prove to be useful in identifying the location of the loop (Figure 4a). The basis of the discrimination relies on size exclusion effects between O_2 and NiEDDA at the site in question. Such discrimination apparently occurs

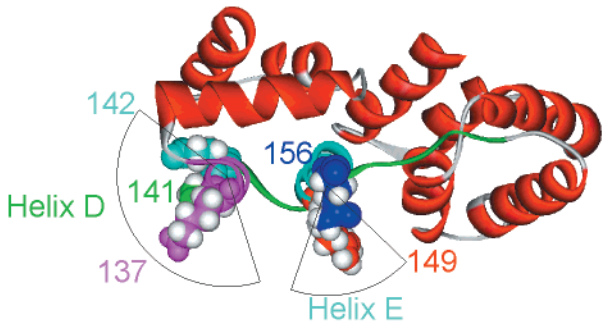

FIGURE 9: Model of helix/surface sites in annexin 12. The indicated helix/surface sites are shown with space filling models, and the solvent-exposed surface of the helix is denoted by the pie-shaped sector. Helix D has a much larger solvated surface. Only repeats 2 and 3 are shown.

only for the most buried sites in the structure. Thus, for loop sites at which R1 has at least one population of high accessibility, or has partial solvent accessibility, there will be little size exclusion and Φ will be approximately constant through the loop sequence. On the other hand, for buried sites in helices D and E, size exclusion effects are important, and Φ increases dramatically (Figure 4A, bottom panel). Thus, Φ is flat at all but helix/buried sites, where local maxima are observed. If a site on a rigid loop were completely buried, this method would fail.

Effects of Backbone Dynamics. A common theme underlying the data of the helix−loop−helix scan is a clear difference between helices D and E. For example, the helical periodicity evident in Π(NiEDDA), $\Pi(O_2)$, and ΔH_o^{-1} is modulated by a low-frequency mode that is maximal in helix D and the loop and minimal in helix E. This indicates that the buried residues in helix D are more mobile and more accessible than those in helix E. It is particularly striking that the polar NiEDDA has access to buried sites in D but essentially not at all in E. In addition, the noninteracting components of the helix/surface sites in helix D have an order parameter much lower than those of helix E. Detailed studies of such sites indicated that variations in the order parameter for R1 between helices were likely due to backbone fluctuations (*18*). Together, these differential effects suggest a more dynamic and loosely packed state for helix D than for helix E. In the annexin 12 structure, helix D has a larger solvent-exposed area than helix E, as indicated in Figure 9, and concomitantly a smaller buried surface. This, together with the shorter length of helix D, may account for the observed differences.

Why should the EPR spectra of the R1 side chain reflect backbone motion? Crystal structures of T4L containing R1 revealed that its disulfide moiety interacts with main chain atoms, effectively eliminating rotations about the disulfide and bonds proximal to the backbone. Detailed studies of noninteracting helix/surface sites showed that the internal motion of R1 was restricted to the two terminal bonds next to the nitroxide ring, consistent with the model derived from crystal structures. Furthermore, simulations based on this model were found to accurately account for the experimental line shapes, and revealed that the motion of R1 on helices is intrinsically ordered (*18*). Because the internal motion is ordered, the spectra are very sensitive to additional degrees of freedom that modulate the internal modes, namely, backbone fluctuations.

The helix/surface spectrum of 149R1 in helix E is unusual in that it has a relatively large $2A_{perp}$ but narrow line widths. This spectral line shape can be simulated assuming a single spin population of highly anisotropic motion (L. Columbus and W. L. Hubbell, unpublished data). Similar spectra have been observed in T4L, and at one site (T4L75), the higher order was found to be due to an unusual hydrogen bond made between a nearby tyrosine and the 4-H atom on the nitroxide ring (*33*). Although there is no tyrosine present in the neighborhood of 149R1, 189E is in a position to make such a hydrogen bond with 149R1.

It is difficult to obtain dynamics information from crystal structures of proteins for several reasons. First, the X-ray structure represents a time-average static protein conformation. Furthermore, the presence of numerous packing interactions between different protein molecules in the crystal will complicate the interpretation. For example, in annexin 12 crystals, helix D in repeat 2 is involved in multiple contacts with neighboring proteins that are likely to dampen the backbone motion. This could explain why this region of the protein in crystals is a well-defined helix with relatively low thermal factors (*22*) yet appears to be dynamic in solution when analyzed in EPR experiments (Figures 4 and 6). In contrast, both EPR and X-ray studies showed that helix E was highly ordered. The notion of a highly dynamic helix D and an ordered E helix is consistent with a recent NMR study in which the structure of an individual repeat domain of annexin I was investigated (*24*). Furthermore, comparison of the X-ray structures of full-length (*34*) and N-terminally truncated annexin I (*35*) demonstrates that the N-terminal domain is able to displace and thereby unfold helix D in repeat 3. Thus, these data suggest that helix D might only be loosely folded and that its interactions with the rest of the protein are likely to be weak. The origin for the different dynamics of helices D and E in solution is unknown; however, it appears likely that the different lengths of the helices (eight amino acids in helix D and 11 amino acids in helix E) and the number of stabilizing side chain interactions might have significant contributions.

The dynamic nature of helix D in solution could have some important implications for the membrane interactions of annexin 12. In the presence of calcium, annexin 12 binds to the surface of phosphatidylserine-containing membranes while maintaining an overall fold similar to that of the crystal structure (our unpublished results). This annexin 12 membrane interaction is highly specific and cooperative, but relatively low in affinity since high calcium concentrations ($\sim 10^{-5}$ M) are required (*36*). Highly specific low-affinity interactions are quite common in biology and are often mediated by disordered protein regions that become ordered only upon binding to another protein or ligand. By using extended stretches of protein for multiple-contact interactions, it is possible to ensure high specificity (enthalpy). To ensure a regulated, reversible interaction, the overall free energy for this interaction is significantly reduced by the entropy loss that is a consequence of the "freezing out" of protein conformations. It is very likely that such a mechanism is also present in annexin 12 considering that the Ca^{2+}-dependent membrane interaction strongly reduces mobility in helix D and the loop connecting helices D and E (our unpublished results).

The dynamic nature of helix D could also be important for the pH-dependent membrane interaction of annexin 12. We recently used a nitroxide scanning experiment to show that the hairpin of helices D and E of repeat 2 in annexin 12 undergoes a pH- and membrane-dependent refolding (*26*). This refolding results in the breakage of all hydrophobic interactions that stabilize the hairpin in solution and the formation of a single, continuous, membrane-inserted helix. The refolding might be facilitated by the loose and dynamic nature of helix D.

ACKNOWLEDGMENT

We thank Drs. Linda Columbus, Peter Qin, and Christian Altenbach for critical comments on the manuscript and Dr. Christian Altenbach for providing the Fourier transforms of Figures 4 and 6. The excellent technical assistance of Elizabeth Baer in the production of the site-directed mutants is gratefully acknowledged.

REFERENCES

1. Hubbell, W. L., and Altenbach, C. (1994) *Curr. Opin. Struct. Biol. 4*, 566−573.
2. Hubbell, W. L., Mchaourab, H. S., Altenbach, C., and Lietzow, M. A. (1996) *Structure 4*, 779−783.
3. Hubbell, W. L., Gross, A., Langen, R., and Lietzow, M. A. (1998) *Curr. Opin. Struct. Biol. 8*, 649−656.
4. Hubbell, W. L., Cafiso, D. S., and Altenbach, C. (2000) *Nat. Struct. Biol. 7*, 735−739.
5. Feix, J. B., and Klug, C. S. (1998) in *Biological Magnetic Resonance, Vol. 14: Spin Labeling: The Next Millenium* (Berliner, L. J., Ed.) pp 252−281, Plemum Press, New York.
6. Altenbach, C., Froncisz, W., Hyde, J. S., and Hubbell, W. L. (1989) *Biophys. J. 56*, 1183−1191.
7. Altenbach, C., Marti, T., Khorana, H. G., and Hubbell, W. L. (1990) *Science 248*, 1088−1092.
8. Margittai, M., Fasshauer, D., Pabst, S., Jahn, R., and Langen, R. (2001) *J. Biol. Chem. 276*, 13169−13177.
9. Oh, K. J., Zhan, H., Cui, C., Altenbach, C., Hubbell, W. L., and Collier, R. J. (1999) *Biochemistry 38*, 10336−10343.
10. Salwinski, L., and Hubbell, W. L. (1999) *Protein Sci. 8*, 562−572.
11. Gross, A., Columbus, L., Hideg, K., Altenbach, C., and Hubbell, W. L. (1999) *Biochemistry 38*, 10324−10335.
12. Klug, C. S., Eaton, S. S., Eaton, G. R., and Feix, J. B. (1998) *Biochemistry 37*, 9016−9023.
13. Merianos, H. J., Cadieux, N., Lin, C. H., Kadner, R. J., and Cafiso, D. S. (2000) *Nat. Struct. Biol. 7*, 205−209.
14. Mchaourab, H. S., Lietzow, M. A., Hideg, K., and Hubbell, W. L. (1996) *J. Biol. Chem. 273*, 810−812.
15. Perozo, E., Cortes, D. M., and Cuello, L. G. (1998) *Nat. Struct. Biol. 5*, 459−469.
16. Voss, J., He, M. M., Hubbell, W. L., and Kaback, H. R. (1996) *Biochemistry 35*, 12915−12918.
17. Poirier, M. A., Xiao, W., Macosko, J. C., Chan, C., Shin, Y. K., and Bennett, M. K. (1998) *Nat. Struct. Biol. 5*, 765−769.
18. Columbus, L., Kalai, T., Jeko, J., Hideg, K., and Hubbell, W. L. (2001) *Biochemistry 40*, 3828−3846.
19. Seaton, B. A. (1996) in *Annexins: Molecular Structure to Cellular Function* (Seaton, B. A., Ed.) R. G. Landes Co., Austin, TX.
20. Gerke, V., and Moss, S. E. (1997) *Biochim. Biophys. Acta 1357*, 129−154.
21. Liemann, S., and Huber, R. (1997) *Cell. Mol. Life Sci. 53*, 516−521.
22. Luecke, H., Chang, B. T., Mailliard, W. S., Schlaepfer, D. D., and Haigler, H. T. (1995) *Nature 378*, 512−515.

23. Altenbach, C., Greenhalgh, D. A., Khorana, H. G., and Hubbell, W. L. (1994) *Proc. Natl. Acad. Sci. U.S.A. 91*, 1667−1671.
24. Cordier-Ochsenbein, F., Guerois, R., Baleux, F., Huynh-Dinh, T., Lirsac, P. N., Russo-Marie, F., Neumann, J. M., and Sanson, A. (1998) *J. Mol. Biol. 279*, 1163−1175.
25. Langen, R., Isas, J. M., Lueke, H., Haigler, T. H., and Hubbell, W. L. (1998) *J. Biol. Chem. 273*, 22453−22457.
26. Langen, R., Isas, J., Hubbell, W., and Haigler, H. (1998) *Proc. Natl. Acad. Sci. U.S.A. 95*, 14060−14065.
27. Hubbell, W. L., Froncisz, W., and Hyde, J. S. (1987) *Rev. Sci. Instrum. 58*, 1879−1886.
28. Oh, K. J., Altenbach, C., Collier, R. J., and Hubbell, W. L. (2000) *Methods Mol. Biol. 145*, 147−169.
29. Altenbach, C., Flitsch, S. L., Khorana, H. G., and Hubbell, W. L. (1989) *Biochemistry 28*, 7806−7812.
30. Koradi, R., Billeter, M., and Wuthrich, K. (1996) *J. Mol. Graphics 14*, 51−55, 29−32.
31. Freed, J. H. (1976) *Spin Labeling Theory and Applications*, Academic Press, New York.
32. Griffith, O. H., Dehlinger, P. J., and Van, S. P. (1974) *J. Membr. Biol. 15*, 159−192.
33. Langen, R., Oh, K. J., Cascio, D., and Hubbell, W. L. (2000) *Biochemistry 39*, 8396−8405.
34. Rosengarth, A., Gerke, V., and Luecke, H. (2001) *J. Mol. Biol. 306*, 489−498.
35. Weng, X., Luecke, H., Song, I. S., Kang, D. S., Kim, S. H., and Huber, R. (1993) *Protein Sci. 2*, 448−458.
36. Schlaepfer, D. D., Fisher, D. A., Brandt, M. E., Bode, H. R., Jones, J. M., and Haigler, H. T. (1992) *J. Biol. Chem. 267*, 9529−9539.

BI011856Z